RESEARCH PAPER

Study on Concrete-Filled CFRP-Steel Tubular Beam-Column with Square Cross-Section

Qing-li Wang[1] · Chang-zhi Duan[1] · Kuan Peng[2] · Yong-bo Shao[2]

Abstract

Tests on twenty-four concrete-filled CFRP-steel tubular beam-columns with square cross-section are conducted (S-CF-CFRP-ST). The experimental consequences show that the axial compression-deflection curve on the cross-section at the mid-height of the composite beam-column could be classified into three stages, i.e., the elastic stage, the elasto-plastic stage and the softening stage, and the failure mode of the specimen is ductile. Analyses show that the CFRP and the steel tube can work together in both longitudinal and transverse directions during the entire loading process, and the longitudinal strains in the steel tube along the depth of the mid-height cross-section are satisfied with the plane section assumption. Furthermore, the steel tube under longitudinal tension has little confinement effect on its nearby concrete. Finite element model is built to predict the deformed mode and the curves of axial compression-deflection of the members. The predicted results agree well with the tested ones. Simultaneously, the effects of several factors on the static performance of these composite members are investigated. Equation for calculating the strength of S-CF-CFRP-ST beam-column is suggested, and the rationality of the presented equation is estimated through comparison of the predicted results with the tested ones.

1 Introduction

Due to the advantage of high strength of concrete material in tri-axial compression, concrete-filled tubular (CFT) structure, in which concrete is confined by the outer tube, has wide applications in civil engineering. Traditional CFT structures include concrete-filled steel tubular (CFST) structure and the concrete-filled fiber reinforced plastic tubular (CF-FRP-T) structure (Nie et al. 2014). However, the durability and bearing capacity of concrete-filled steel tube are easily affected by the corrosion of the outer wall in the process of use. CFRP (carbon fiber-reinforced plastic) is widely used in civil engineering because of its lightweight, high strength and good corrosion resistance (Yuan 2016). Concrete-filled carbon fiber-reinforced plastic-steel tubular (CF-CFRP-ST) is a new type of composite structure which combines the merits of CFST and CF-CFRP-T, and it can be considered as a good choice to increase the durability of CFST. Both CF-CFRP-ST and CFST are used to improve the bearing capacity of the specimen by the restraint effect of the outer tube. The existence of CFRP can delay the buckling deformation of the steel tube and improve the ductility of the specimen (Che et al. 2012).

Park et al. (2011) tested the axial compression performance of S-CF-CFRP-ST, and the main parameters of the test were the number of CFRP layers. The test results show that the local buckling of the steel tube is delayed by CFRP,

✉ Kuan Peng
  pklut7@163.com

  Qing-li Wang
  wql@ustl.edu.cn

  Chang-zhi Duan
  Doris98@126.com

  Yong-bo Shao
  252833213@qq.com

[1] School of Civil Engineering, University of Science and Technology LiaoNing, No.189 Qianshan Middle Road, Lishan District, Anshan 114051, Liaoning Province, People's Republic of China

[2] School of Mechatronic Engineering, Southwest Petroleum University, No.8 Xindu Avenue, Xindu District, Chengdu 610500, Sichuan Province, People's Republic of China

and the bearing capacity of the specimen increases with the increase in CFRP layers. Al Zand et al. (2015) studied the performance change of square CFRP concrete-filled steel tubular (CFST) flexural members through finite element simulation. It was found that CFRP has little effect on the flexural capacity of CFST in the elastic stage, but has a greater impact on the plastic stage. There were also some studies on CF-CFRP-ST, such as cyclic performance by Tao et al. (2007a, b) and Cai et al. (2016), enhancement performance by Al Zand et al. (2016), dynamic behavior, delamination failure and rectangular specimens by Alam et al. (Wang and Shao 2015; Wang et al. 2016, 2018; Li et al. 2016; Park et al. 2010) and slenderness effects by Li et al. (2018). However, most of these were mainly focused on the compressive and flexural performances of the composite members. In practice, CF-CFRP-ST may be subjected to bending moment besides axial compression such as the engineering example shown in Fig. 1, which indicates that it is necessary to carry out research on CF-CFRP-ST beam-column.

Based on the above introduction, tests on twenty-four S-CF-CFRP-ST beam-columns were carried out in this study. The curves of axial compression (N)-deflection (u_m) on cross-section at the mid-height of the specimens were obtained, and the cooperation between the CFRP and the steel tube, applicability of plane section assumption and so on for the S-CF-CFRP-ST beam-columns are discussed. The failure process and the failure modes of the S-CF-CFRP-ST beam-columns were also simulated by using finite element (FE) software ABAQUS. In addition, the behavior of the S-CF-CFRP-ST beam-column was investigated in details through the analyses of the influence of the eccentricity ratio, the slenderness ratio, the number of layers of the longitudinal CFRP and the transverse CFRP, the yield strength of steel, the strength of concrete and the steel ratio on the static response. Finally, a set of parametric equations for

calculating the load-carrying capacity of the S-CF-CFRP-ST beam-columns were proposed and verified.

2 Experimental Investigation

2.1 General

Twenty-four S-CF-CFRP-ST beam-column specimens were tested, and the key parameters include slenderness ratio (λ) and eccentricity ratio (e). λ and e herein are defined by the following equation

$$\lambda = 2\sqrt{3}L/B \tag{1}$$

$$e = 2e_0/B \tag{2}$$

where L is the height of the specimen; B is the side-length of the steel tube (B of each specimen is 140 mm); e_0 is the eccentricity, it refers to the distance from the application point of force to the centroid of section; eccentricity ratio (e) reflects the relationship between eccentricity and component size; λ has a direct relationship with the calculated length and side length of specimens, which is an important factor reflecting the stability of the component (Wang and Niu 2017; Wang and Sw 2019);

Table 1 contains the rest parameters of the specimens.

2.2 Material Properties and Specimen Preparations

Cold-formed steel tube was adopted, radius of the inner rounding chamfer is 5 mm, and the properties of the steel tube obtained from tensile tests are listed in Table 1. Test standards of steel performance can be referenced by Che et al. (2012).

Cement, sand, water and coarse aggregate are used as raw materials of concrete. The ratio of cement, sand, water and coarse aggregate is 485:703:150:1062. f_{cu} is obtained from compressive tests of concrete cubes with the dimension 150 mm × 150 mm × 150 mm. The elastic modulus (E_c) and Poisson's ratio (v_c) of the concrete are assumed to be 35.9GPa and 0.22. Test standards of concrete performance can be reference from code for design of concrete in China (Wang et al. 2016).

The properties of the CFRP were listed as follows: the tensile strength $f'_{cf} = 4.83$ GPa, the elastic modulus $E_{cf} = 230$ GPa, the elongation percentage $\delta_{cf} = 21\%$, the density $w_{cf} = 200$ g•m^{-2}, and the thickness $t_{cf} = 0.111$ mm.

Specimen preparations can be referenced to S-CF-CFRP-ST columns adopted by Wang et al. (Sundarraja and Ganesh 2012).
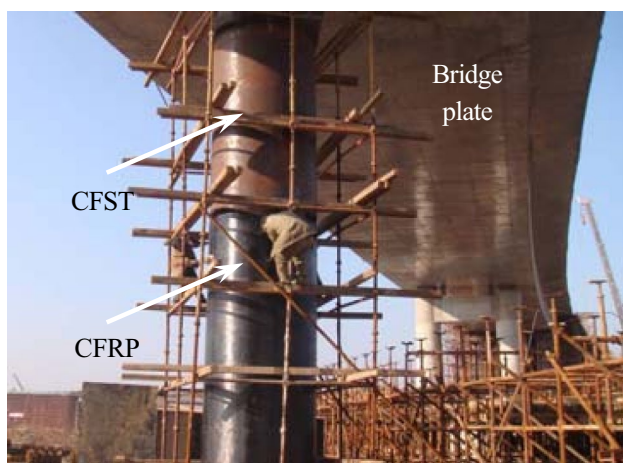

Fig. 1 C-CF-CFRP-ST used in engineering practice

Table 1 Details of specimens

No.	Specimens label	L (mm)	λ	e_0 (mm)	t_s (mm)	f_u (MPa)	f_y (MPa)	v_s	E_s (GPa)	f_{cu} (MPa)	f_{ck} (MPa)	N_{bc}^t (kN)
1	SBC A-0	420	10.4	0	3.5	425	300	0.28	203	49	32.83	1475
2	SBC A-14	420	10.4	14	3.5	425	300	0.28	203	49	32.83	1195
3	SBC A-28	420	10.4	28	3.5	425	300	0.28	203	49	32.83	1045
4	SBC A-42	420	10.4	42	3.5	425	300	0.28	203	49	32.83	905
5	SBC B-0	630	15.6	0	3.5	425	300	0.28	203	49	32.83	1470
6	SBC B-14	630	15.6	14	3.5	425	300	0.28	203	49	32.83	1170
7	SBC B-28	630	15.6	28	3.5	425	300	0.28	203	49	32.83	1040
8	SBC B-42	630	15.6	42	3.5	425	300	0.28	203	49	32.83	825
9	SBC C-0	840	20.8	0	3.5	425	300	0.28	203	49	32.83	1390
10	SBC C-14	840	20.8	14	3.5	425	300	0.28	203	49	32.83	1175
11	SBC C-28	840	20.8	28	3.5	425	300	0.28	203	49	32.83	935
12	SBC C-42	840	20.8	42	3.5	425	300	0.28	203	49	32.83	830
13	SBC D-0	1260	31.2	0	3.5	425	300	0.28	203	49	32.83	1335
14	SBC D-14	1260	31.2	14	3.5	425	300	0.28	203	49	32.83	985
15	SBC D-28	1260	31.2	28	3.5	425	300	0.28	203	49	32.83	850
16	SBC D-42	1260	31.2	42	3.5	425	300	0.28	203	49	32.83	745
17	SBC E-0	1680	41.6	0	3.5	425	300	0.28	203	49	32.83	1270
18	SBC E-14	1680	41.6	14	3.5	425	300	0.28	203	49	32.83	915
19	SBC E-28	1680	41.6	28	3.5	425	300	0.28	203	49	32.83	805
20	SBC E-42	1680	41.6	42	3.5	425	300	0.28	203	49	32.83	695
21	SBC F-0	2520	62.4	0	3.5	425	300	0.28	203	49	32.83	1162
22	SBC F-14	2520	62.4	14	3.5	425	300	0.28	203	49	32.83	851
23	SBC F-28	2520	62.4	28	3.5	425	300	0.28	203	49	32.83	712
24	SBC F-42	2520	62.4	42	3.5	425	300	0.28	203	49	32.83	639

where t_s is the wall thickness of the steel tube; L is the height of the specimen; f_u, f_y, v_s and E_s are the ultimate strength, the yield strength, the Poisson's ratio and the elastic modulus of the steel, respectively; f_{cu} and f_{ck} are the compressive strength and the characteristic compressive strength of the concrete cube respectively, and $f_{ck} = 0.67 f_{cu}$; N_{bc}^t is the test value of the axial compressive load-carrying capacity (N_{bc}) of the S-CF-CFRP-ST beam-column. For all the tested C-CF-CFRP-ST specimens, two layers of CFRP are bonded on outer surface of steel tube. The fiber direction of the first layer CFRP is along the axial direction of specimen, and the second layer is along the circumferential direction of specimen

2.3 Test Setup and Instrumentation

The experimental test is carried out at the Structural Engineering Laboratory of Shenyang Jianzhu University. The test setup is shown in Fig. 2.

The specimen was pinned at both ends. A hydraulic machine with a loading capacity of 5000 kN was used to apply axial compression N with different e_0 (Wang and Chen 2014). The load was applied in several steps. In the elastic stage, each loading step was 1/10 of the estimated ultimate load. The estimated ultimate load was obtained by the following method: all the CFRPs were transferred into the steel tube based on equivalent strength, and the transverse CFRP has restraint effect, so it is calculated as confinement factor (ξ_{cf}). The longitudinal CFRP has no restraint effect, but has a certain longitudinal reinforcement effect, so it is calculated as strengthening factor η

In the research work on CF-CFRP-ST, the confinement of the steel tube to the concrete is represented by a confinement factor ξ_s.

$$\xi_s = A_s f_y / \left(A_c f_{ck} \right) \tag{3}$$

where A_s is the cross-sectional area of the steel tube and A_c is the cross-sectional area of the concrete.

Similarly, the confinement of the transverse CFRP can also be represented by a confinement factor ξ_{cf} proposed by Wang and Shao (2014). Because the longitudinal CFRP has no restraint effect on the members, the equivalent steel tube transferred from the longitudinal CFRP was not considered in calculating the confinement factor of the steel tube ξ_{cf} presented. However, longitudinal CFRP increases cross-sectional area of specimen. The strengthening efficiency of the longitudinal CFRP can be represented by a strengthening
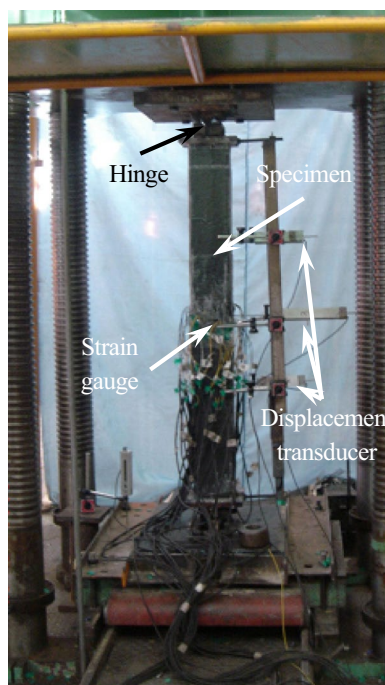
Fig. 2 Test setup

Fig. 3 Location of strain gauges

glued on the surfaces of each steel tube and the CFRP on the cross-section at the mid-height of the specimens, respectively. 5 longitudinal strain gauges were used to measure longitudinal strain, and 5 transverse strain gauges were used to measure transverse strain in steel tube and CFRP, respectively. The data were captured and saved by Data Acquisition System U-CAM-70A, and the N-u_{m} curve was recorded at the same time.

2.4 Test Observations

In the initial loading stage, elastic deformation is observed in the S-CF-CFRP-ST beam-column, and the increase in the deflection is proportional to the loading increase. At this moment, the global deformation is not very visible. With continuous loading process, the sound of CFRPs' splitting can be heard. The global deformation becomes clearly visible, and a convex deformation occurs in the compressive region at the mid-height, as shown in Fig. 4a. Then $N_{\mathrm{bc}}{}^{\mathrm{t}}$ is reached. Since then, the eccentricity ratio and the slenderness ratio will influence the failure process.

For the members with smaller slenderness ratio and eccentricity ratio, the transverse CFRP at the corner of the compressive region is fractured firstly as shown in Fig. 4b, while the longitudinal CFRP in the tensile region is generally not fractured. For the specimens with relatively smaller slenderness ratio and larger eccentricity ratio, either the transverse CFRP in the compressive region or the longitudinal CFRP in the tensile region is fractured firstly. For the specimens with relatively larger slenderness ratio and smaller eccentricity ratio, the longitudinal CFRP in the tensile region is fractured at a large deflection following the fracture of the transverse CFRP in the compressive region. For the specimens with a larger value of both the slenderness ratio and the eccentricity ratio (Fig. 4c), the longitudinal CFRP in the tensile region is firstly fractured at a large deflection, while the transverse CFRP in the compressive

factor η in the process of calculating the estimated ultimate load (Wang et al. 2015). The definitions of all the above confinement or strengthening factors are provided as follows:

$$\xi_{\mathrm{cf}} = A_{\mathrm{cft}} f_{\mathrm{cft}} / \left(A_{\mathrm{c}} f_{\mathrm{ck}} \right) \tag{4}$$

$$\eta = A_{\mathrm{cfl}} f_{\mathrm{cfl}} / \left(A_{\mathrm{s}} f_{\mathrm{y}} \right) \tag{5}$$

$$f_{\mathrm{cft}} = E_{\mathrm{cf}} \varepsilon_{\mathrm{cftr}} = 690 \text{ MPa} \tag{6}$$

$$f_{\mathrm{cfl}} = E_{\mathrm{cf}} \varepsilon_{\mathrm{cflr}} = 2300 \text{ MPa} \tag{7}$$

where A_{cft} and f_{cft} are the cross-sectional area and the ultimate tensile strength of the transverse CFRP, respectively; A_{cfl} and f_{cfl} are the cross-sectional area and the ultimate tensile strength of the longitudinal CFRP, respectively.

When the applied load reaches about 60% of the estimated load-carrying capacity, the loading increment is reduced to 1/15–1/20 of the estimated ultimate load. After the load-carrying capacity, displacement control is used till the deflection on the cross-section at the mid-height reaches about L/25. The time interval between two loading steps is maintained for about 2–3 min.

According to different heights of the specimens, three to five displacement transducers were used to monitor the deflections. Steel tube and CFRP laminates at five points (point 1~5) of middle height of the specimens pasted twenty strain gauges, as shown in Fig. 3. 10 strain gauges were
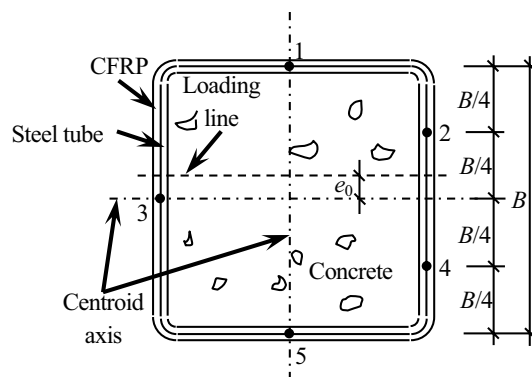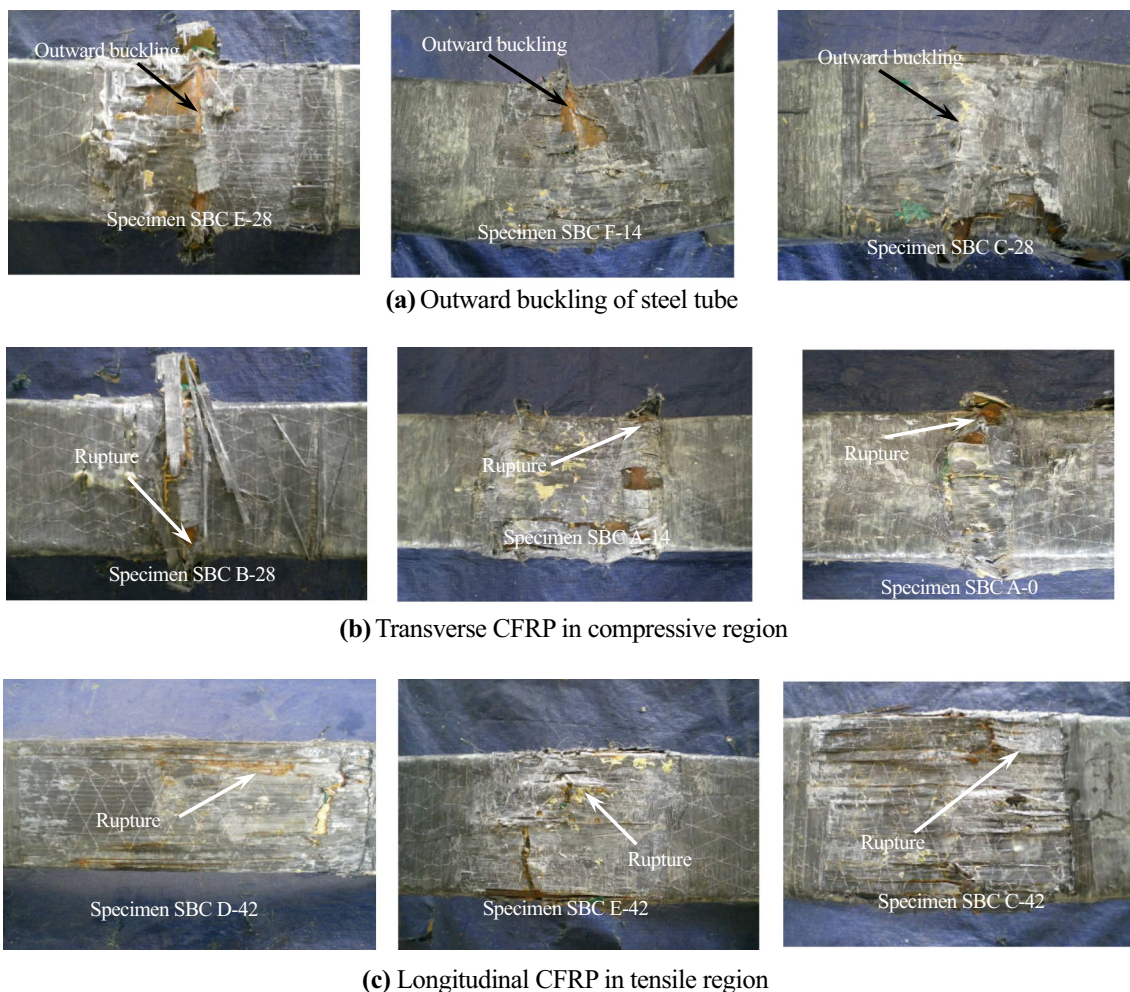
(a) Outward buckling of steel tube

(b) Transverse CFRP in compressive region

(c) Longitudinal CFRP in tensile region

Fig. 4 Outward buckling of steel tube and rupture of CFRPs

Fig. 5 Specimens after loading

region is generally not fractured. Specimens after loading are shown in Fig. 5.

The specimens are cut into two halves after the test. As shown in Fig. 6, it is found that the concrete can be divided into tensile and compressive regions. For the specimens with the same eccentricity ratio, the damage of the concrete becomes more severe when the slenderness ratio reduces. The failure mode is crush of the concrete in the compressive

region (as shown in Fig. 6a). The crack of the concrete in the tensile region is wide as shown in Fig. 6b. The failure of the concrete becomes slighter when the slenderness ratio becomes larger (as shown in Fig. 6c). The crack width of the concrete in the tensile region is narrow as shown in Fig. 6d. For the specimens with the same slenderness ratio, the damage of the concrete becomes slighter and the crack of the concrete in the tensile region is narrower when the eccentricity ratio becomes larger.

All the experimental phenomena observed during test are summarized in Table 2.

2.5 Test Results and Analyses

2.5.1 Curves of Axial Compression-Deflection on Cross-Section at Mid-Height

The tested N-u_m curves of all specimens are shown in Fig. 7. The characteristics of the curves are listed as follows: In the

Fig. 6 Failure modes of concrete

(a) Concrete in compressive region of specimen SBC D-42

(b) Concrete in tensile region of specimen SBC C-42

(c) Concrete in compressive region of specimen SBC F-42

(d) Concrete in tensile region of specimen SBC E-42
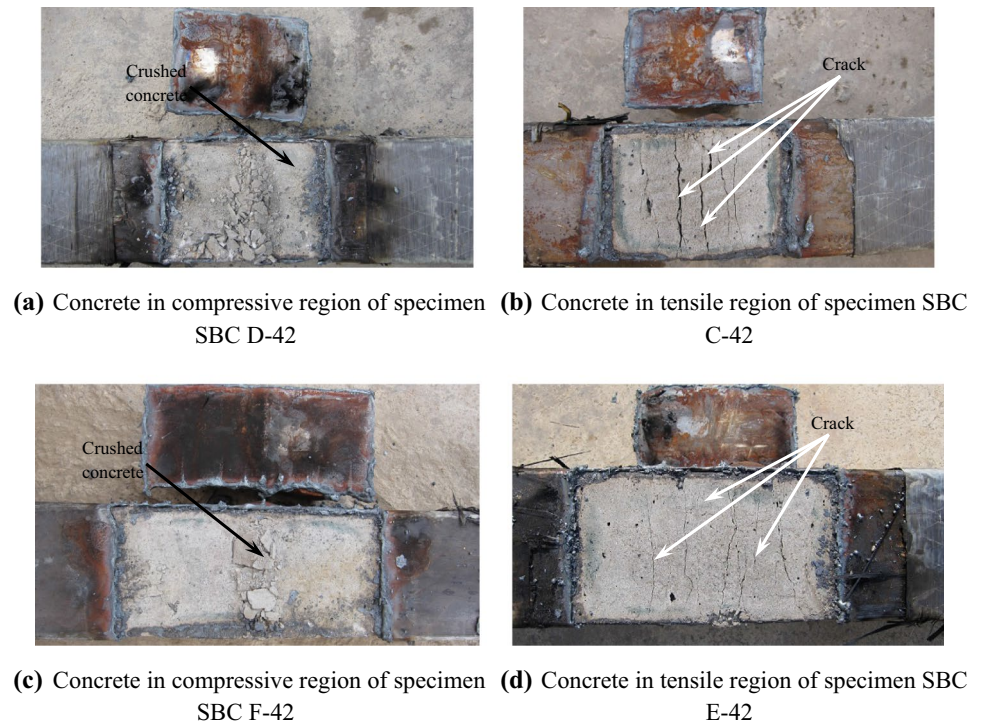
Table 2 Summary of test observations

Evaluating Indicator	Small eccentricity ratio	Large eccentricity ratio
Small slenderness ratio (The failure modes tend to be yield failure)	The transverse CFRP at the corner of the compressive region is fractured firstly while the longitudinal CFRP in the tensile region is generally not fractured	Either the transverse CFRP in the compressive region or the longitudinal CFRP in the tensile region is fractured firstly
Large slenderness ratio (The failure modes tend to be instability state, and there are no obvious characteristics of strength failure)	The longitudinal CFRP in the tensile region is fractured at a large deflection following the fracture of the transverse CFRP in the compressive region	The longitudinal CFRP in the tensile region is firstly fractured at a large deflection while the transverse CFRP in the compressive region is generally not fractured

early loading stage, both the applied load and the deflection are small, and the curves are approximately linear and elastic in this stage. Elasto-plastic stage follows sequentially. After $N_{bc}{}^t$, there is a loading drop in the curve, and the deflection increases rapidly with a gradual loading drop, and the failure at this stage is ductile.

2.5.2 Cooperation Between Steel Tube and CFRP

Figure 8 shows the comparison of the strains between the steel tube and the CFRP, in which ε_{sl} and ε_{st} are the longitudinal strain and the transverse strain of the steel tube, respectively, and ε_{cfl} and ε_{cft} are the strain of the longitudinal CFRP and the transverse CFRP, respectively. As shown in Fig. 8, the values of ε_{sl} and ε_{cfl} are almost the same, as well as ε_{st} and ε_{cft}. Additionally, it is found that the adherence between the CFRP and the steel tube is still intact except

in the region where the CFRP is ruptured, which indicates that the steel tube and the CFRP can cooperate well in both longitudinal and transverse directions.

2.5.3 Comparison Between Longitudinal and Transverse Strains

Figure 9 shows comparisons between ε_{st} and ε_{sl} of Points 1 and 5 for specimen SBC F-14, where ε_s is the strain of the steel tube. It is found that the signs of ε_{sl} and ε_{st} at a same point are different: the transverse strain has a negative value, and the longitudinal strain has a positive value, and vice versa. It is also found from Fig. 9 that Point 5 is under tension, which indicates that the steel tube has no transverse confinement to the inner concrete at this point. Such phenomenon is explained as follows: The concrete around Point 5 is also subjected to tension when the steel tube is under
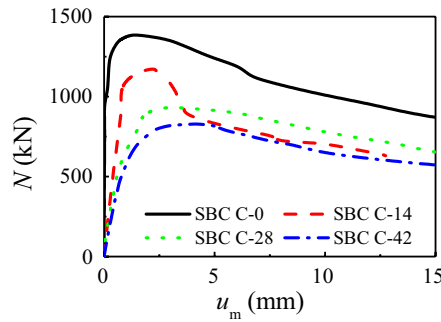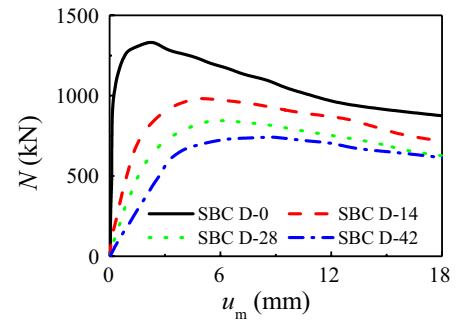
Fig. 7 Tested N-u_m curves
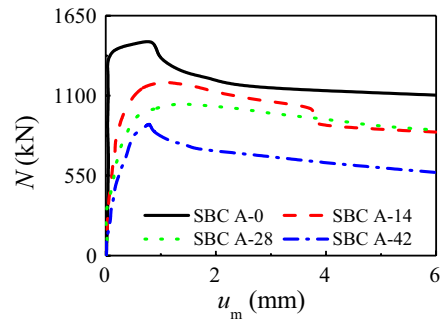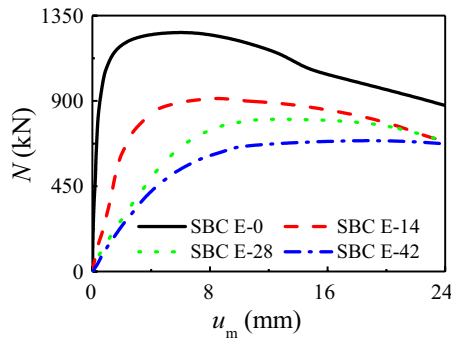

(a) Specimens of λ=10.4
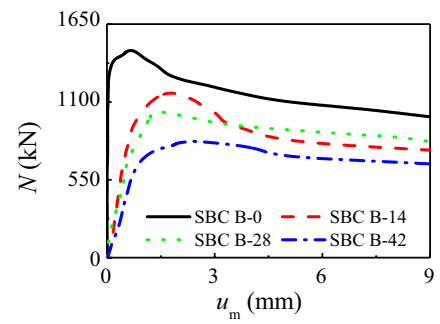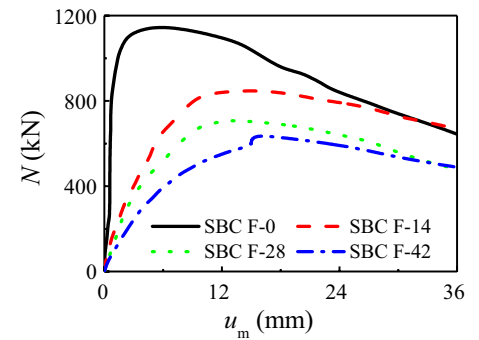
(b) Specimens of λ=15.6

(c) Specimens of λ=20.8

(d) Specimens of λ=31.2

(e) Specimens of λ=41.6

(f) Specimens of λ=62.4

Fig. 8 Comparison between ε_s and ε_{cf}
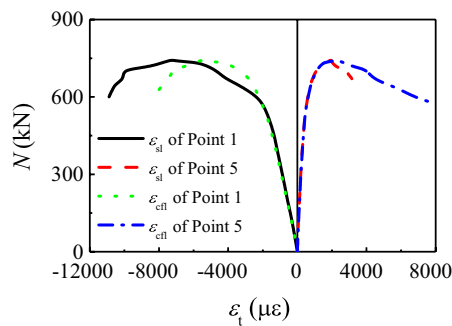
(a) N-ε_l curves of specimen SBC D-42
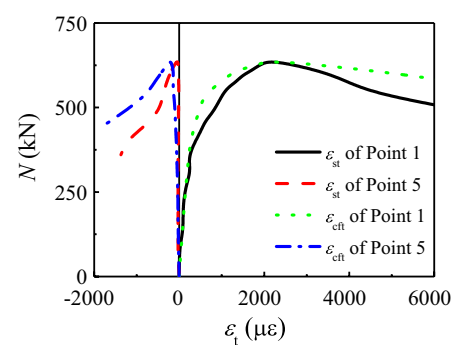
(b) N-ε_t curves of specimen SBC F-42
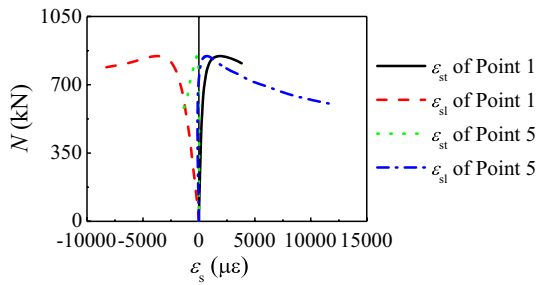
Fig. 9 Comparison between ε_{st} and ε_{sl} of Points 1 and 5 for specimen SBC F-14

longitudinal tension, and hence the steel tube has no need to provide transverse confinement to the concrete. The transverse strain is compressive when the steel tube is subjected to longitudinal tension.

2.5.4 Plane Section Assumption

Figure 10 shows the distribution of ε_{sl} over the depth on the cross-section at the mid-height of the specimen with $\lambda = 41.6$. The distribution of ε_{sl} is basically satisfied with the plane section assumption.

3 Finite Element Simulation

3.1 Constitutive Relationship of Materials

The elasto-plastic model is used, and von Mises criterion is used to evaluate the yielding state. A 4-stage stress–strain relationship of steel suggested by Abdel-Rahman and Sivakumaran (1997) is adopted here, and the cold hardening effect at the corner of the steel tube is modeled by referring to the presented model by Karren (1967). The constitutive relationship of the square CFRP-steel tube confined concrete proposed by Wang and Shao (2014) is used. Through the study of physical properties of CFRP, it is found that the CFRP is subjected tension only. When the CFRP is under compression, the stress it bears is very small, and it can be ignored (Dai and Zhao 2018). The stress of CFRP is defined to be 0.001 MPa in FE model. The constitutive relationship obeys Hooke's Law before fracture as follows:

$$\sigma_{cf} = E_{cf}\varepsilon_{cf} \tag{8}$$

where σ_{cf} and ε_{cf} are the stress and the strain of the CFRP, respectively.

When the longitudinal CFRP reaches its rupture strain ($\varepsilon_{cflr} = 10{,}000$ µε) given by Wang et al. (Sundarraja and Ganesh 2011), it loses longitudinal strengthening effect to
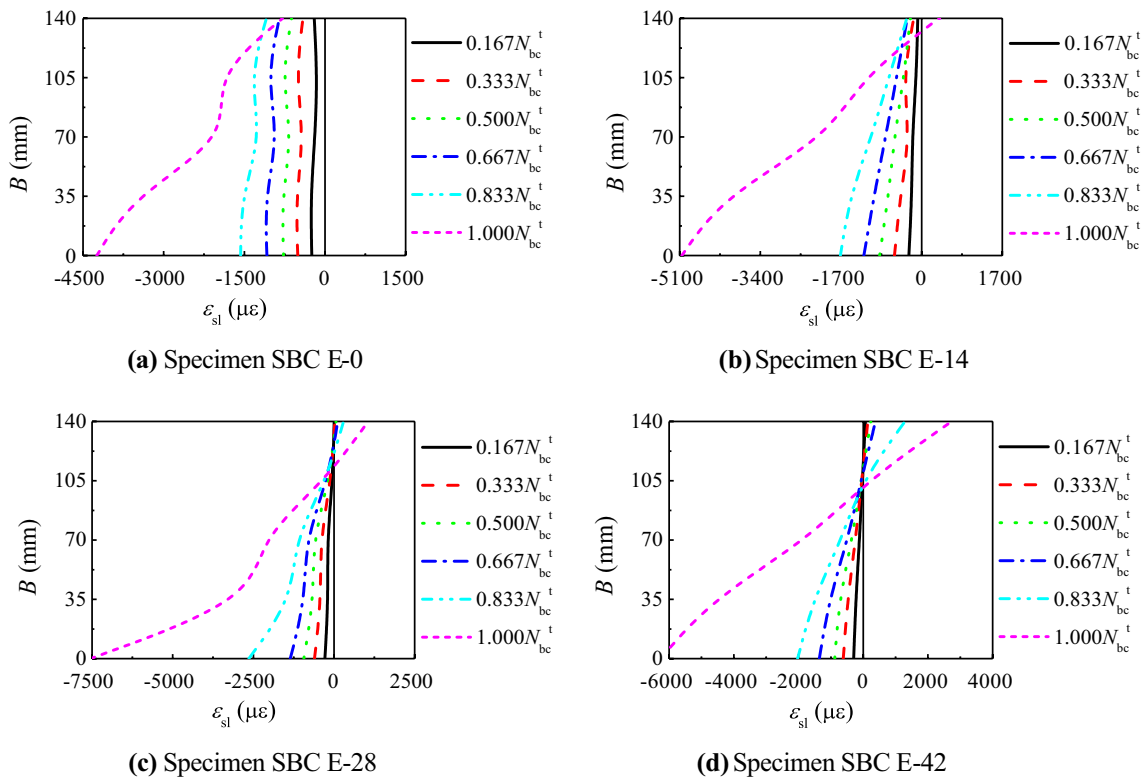

(a) Specimen SBC E-0

(b) Specimen SBC E-14

(c) Specimen SBC E-28

(d) Specimen SBC E-42

Fig. 10 Distribution of ε_{sl} over depth on cross-section at mid-height of specimens with $\lambda = 41.6$

the members. However, the transverse CFRP loses transverse confinement to the steel tube when it reaches the rupture strain ($\varepsilon_{cftr} = 3000 \, \mu\varepsilon$) given by Wang and Shao (2014).

3.2 FE Model

Element selection, mesh discretization, interface model between the steel tube and the concrete, between the end plate and the concrete can be referenced to S-CF-CFRP-ST columns adopted by Wang et al. (2015).

There are three different loading paths for a beam-column, as shown in Fig. 11.

Loading path 1: Apply the axial compression N and keep it constantly, then apply the bending moment M; Loading path 2: Apply the axial force N and the bending moment M simultaneously with a proportional increment; Loading path 3: Apply the bending moment firstly and keep it constantly, and then apply the axial force N. Boundary conditions (as shown in Fig. 12) in the finite element analysis are in accordance with the experimental placement (Loading path 2). According to the symmetry of both geometry and boundary conditions, 1/4 of the entire model is analyzed. Symmetrical constraints are applied on the symmetrical plane of the model. Displacements of x-, y- and z-direction at one end are fixed, and the loading line is placed at the other end. Incremental iteration method by controlling the displacement is used.

3.3 FE Results

3.3.1 Deformed Modes

To examine the reliability of the above FE method, twenty-four S-CF-CFRP-ST beam-columns are analyzed. Figure 13 shows the deformed modes of the member in the experiment and the FE simulation. Figures 14 and 15 show the comparison of Fracture failure mode of CFRP of Specimens SBC C-42 and SBC-B-28, respectively.
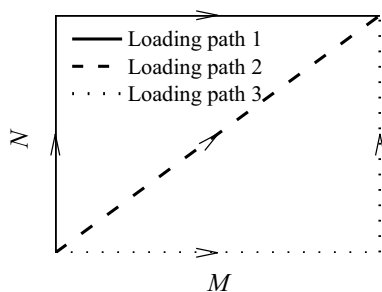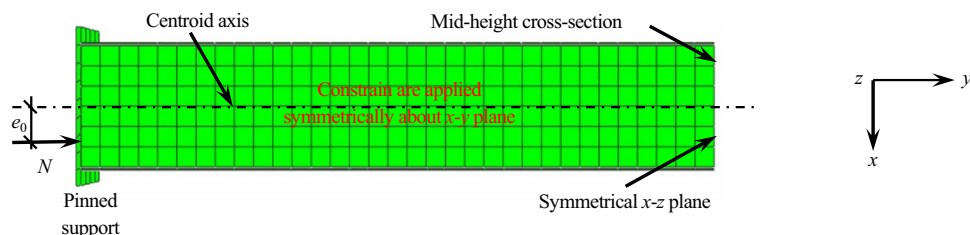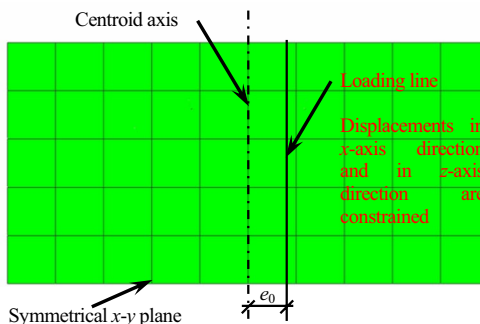

Fig. 11 Loading path of beam-column

Fig. 12 Boundary conditions

(a) Longitudinal direction

(b) End plate

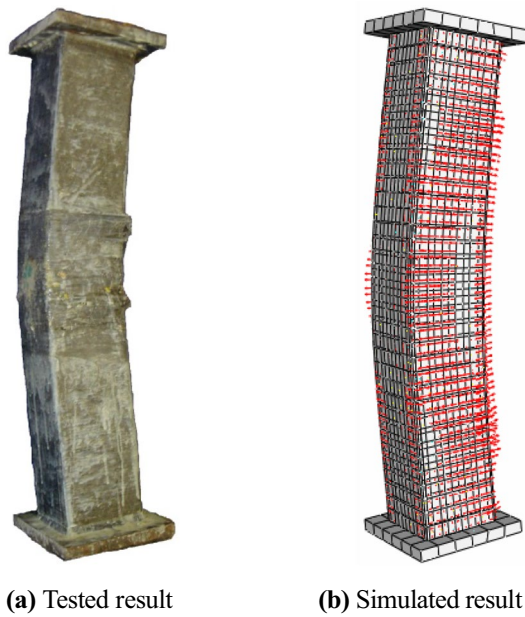**(a)** Tested result **(b)** Simulated result

Fig. 13 Modes of deformation

3.3.2 *N-u*$_m$ Curves

The FE *N-u*$_m$ curves together with the measured results of several specimens are plotted in Fig. 16. Similarly, the FE results also in good agreement with the tested records.

3.4 Parametric Analyses

Possible parameters that will affect the *N-u*$_m$ curves of the S-CF-CFRP-ST beam-columns contain eccentricity ratio, slenderness ratio, number of layer of CFRP, yield strengths of materials and steel ratio. The influences of the above parameters on the *N-u*$_m$ curves of the S-CF-CFRP-ST beam-columns are analyzed by typical examples. Parameters of the typical models are listed as follows: $B = 140$ mm, $t_s = 3.5$ mm, $f_y = 300$ MPa, $f_{cu} = 50$ MPa, $\lambda = 31.2$, $\xi_{cf} = 0.072$, $\eta = 0.249$, $e = 0.4$, $E_s = 206$ GPa, $v_s = 0.3$, $E_c = 4700$ $f'^{0.5}_c$ MPa, where f'_c is the compressive strength of the cylinder concrete.

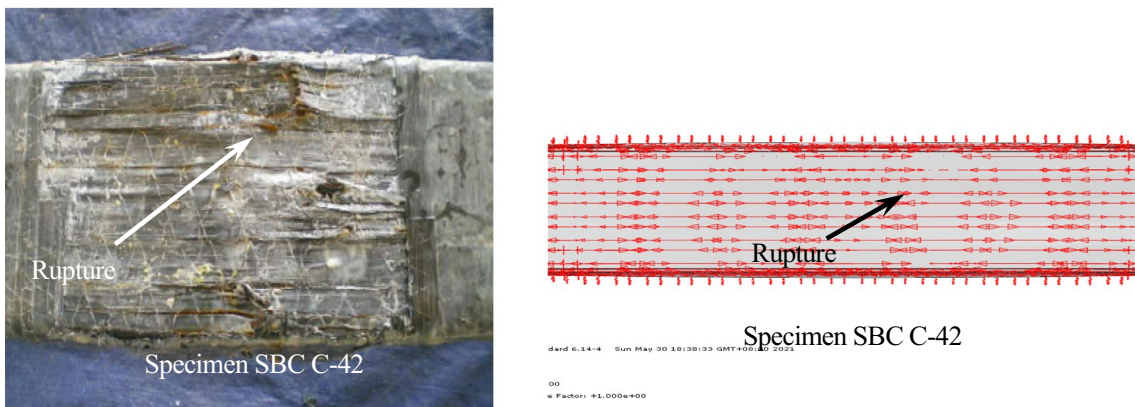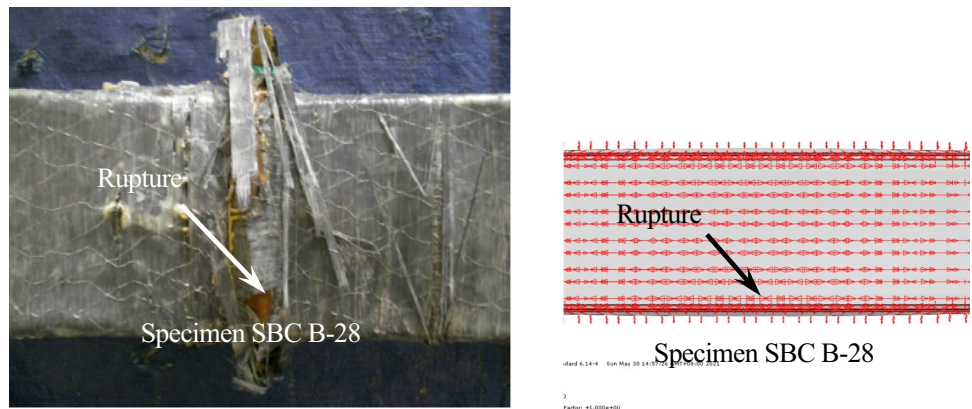**Fig. 14** Comparison of fracture failure mode of CFRP of Specimen SBC B-28

Fig. 15 Comparison of Fracture failure mode of CFRP of Specimen SBC C-42

Fig. 16 Comparison of N-u_m curves between FE results and tested results

(a) Specimen SBC A-28

(b) Specimen SBC B-28

(c) Specimen SBC C-28

(d) Specimen SBC D-28

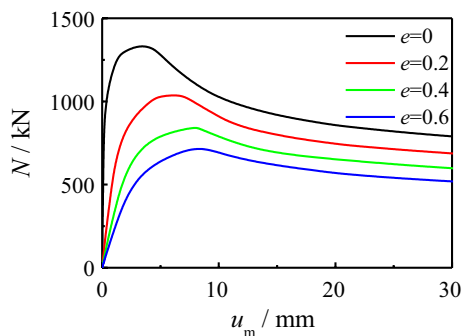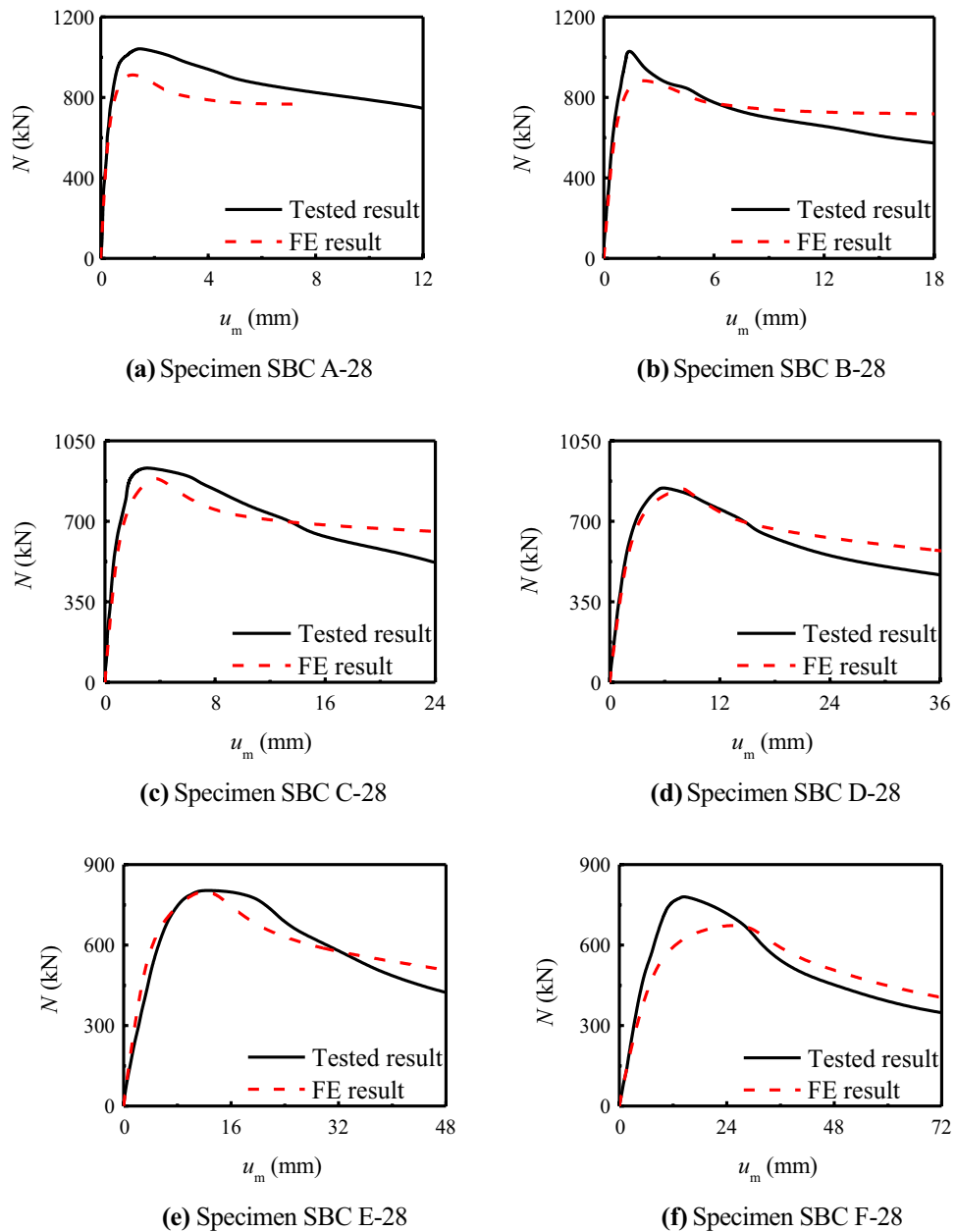**(e)** Specimen SBC E-28

(f) Specimen SBC F-28

Fig. 17 Influence of e on N-u_m curves of S-CF-CFRP-ST beam-columns

Figure 17 shows the influence of the eccentricity ratio on the N-u_m curves of the S-CF-CFRP-ST beam-columns. It can be seen that as e increases, the shape of the curve does not change significantly, and the stiffness of the elastic stage and the load-carrying capacity of the member both reduce significantly. The reason is that the moment increases with the increase of eccentricity ratio, which makes the member more prone to deformation and reduces the bearing capacity.

Figure 18 shows the influence of the slenderness ratio on the N-u_m curves of the S-CF-CFRP-ST beam-columns. It can be seen that as λ increases, the loading-carrying capacity and the stiffness of the elastic stage of the member both reduce significantly, and the shape of the curve changes
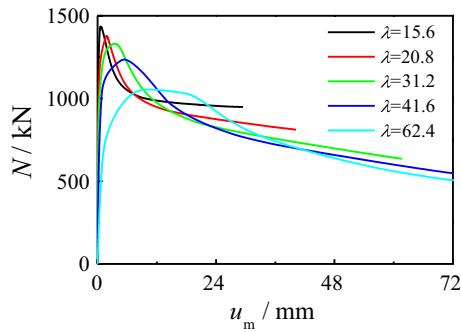
🖄 Springer

Fig. 18 Influence of λ on N-u_m curves of S-CF-CFRP-ST beam-columns

significantly too. The λ has a direct relationship with the length of the specimen. When the slenderness ratio is small, the failure mode is strength failure, and the member with large slenderness ratio easily occurs instability failure under eccentric compression.

Figure 19 shows the influence of the number of layers of the CFRPs on the N-u_m curves of the S-CF-CFRP-ST beam-columns. It can be seen that as m_l or m_t increases, the shape of the curve and the stiffness of the elastic stage change a little. At the same time, the load-carrying

capacity of the member improves slightly and the effect of transverse CFRP is more obvious than that of the longitudinal CFRP. The main reason of such phenomenon is that the longitudinal CFRP has no restraint effect on the bearing capacity of the specimen, but the transverse CFRP has restraint capacity on the specimen, so the change of the number of layers has effect on the bearing capacity.

Figure 20 shows the influence of the strengths of the materials on the N-u_m curves of the S-CF-CFRP-ST beam-columns. It can be seen that as f_y or f_{cu} increases, the shape of the curve and the stiffness of the elastic stage do not change significantly and the load-carrying capacity of the member improves apparently. Because steel tube and concrete are the main components of CF-CFRP-ST, the change of their strength plays a decisive role in the bearing capacity of specimens. Macroscopically, the bearing capacity of members is proportional to f_y and f_{cu}.

Figure 21 shows the influence of the steel ratio on the N-u_m curves of the S-CF-CFRP-ST beam-columns. The steel ratio has a direct relationship with the cross-sectional area of steel tube. With the increase in steel area, the steel ratio increases. It can be seen that as steel ratio (α) increases, the load-carrying capacity of the member improves apparently; however, the shape of the curve does not change.

Fig. 19 Influence of number of layers of CFRPs on N-u_m curves of S-CF-CFRP-ST beam-columns
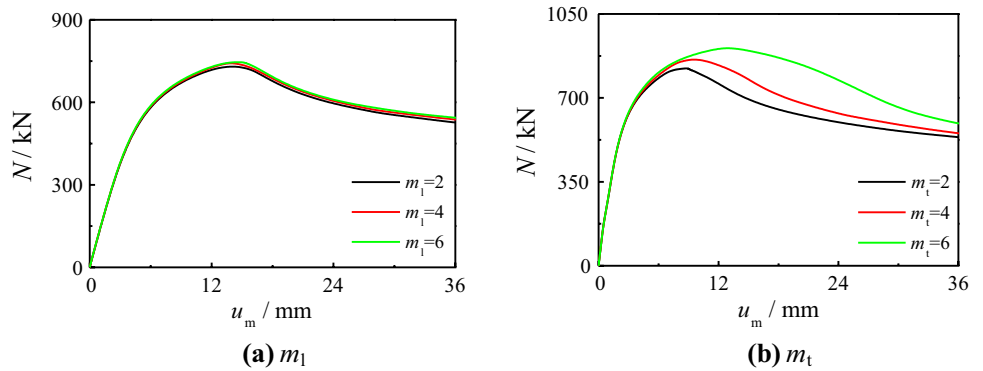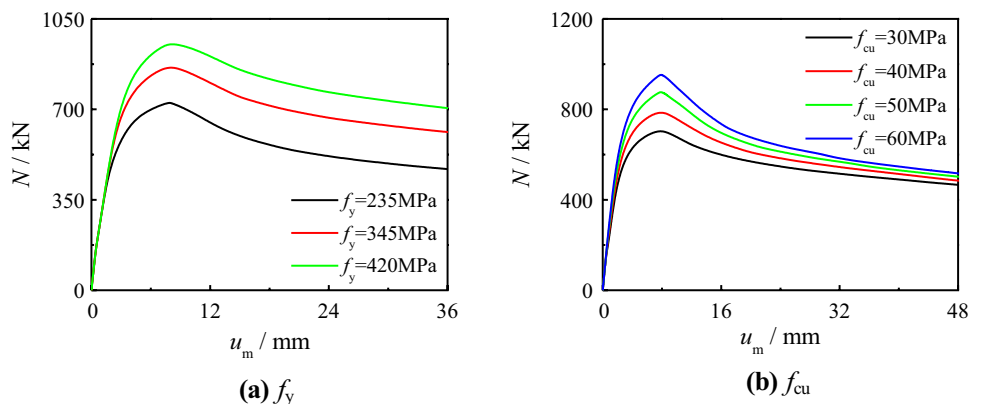

(a) m_l

(b) m_t

Fig. 20 Influence of strengths of materials on N-u_m curves of S-CF-CFRP-ST beam-columns

(a) f_y

(b) f_{cu}
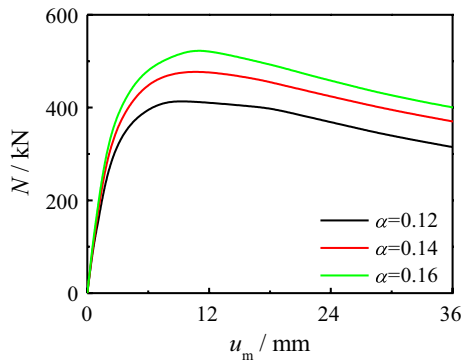
Fig. 21 Influence of α on N-u_m curves of S-CF-CFRP-ST beam-columns
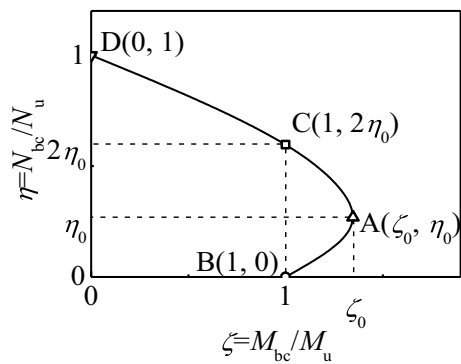
Fig. 22 Typical $N_\mathrm{bc}/N_\mathrm{u}$-$M_\mathrm{bc}/M_\mathrm{u}$ curves

4 Load-Carrying Capacity

4.1 Expression

Figure 22 shows the typical $N_\mathrm{bc}/N_\mathrm{u}$-$M_\mathrm{bc}/M_\mathrm{u}$ curve for an S-CF-CFRP-ST beam-column, where N_u is the load-carrying capacity of the S-CF-CFRP-ST stub column under axial compression, and it is calculated from the presented equations by Wang and Shao (2014); M_u is the flexural load-carrying capacity of the S-CF-CFRP-ST proposed by Wang et al. (2015).

Many calculated results ($f_\mathrm{y} = 200\text{-}400$ MPa, $f_\mathrm{cu} = 30\text{-}120$ MPa, $\xi_\mathrm{s} = 0.2\text{-}4$, $\xi_\mathrm{cf} = 0\text{-}0.6$, $\eta = 0\text{-}0.9$, $E_\mathrm{s} = 206\mathrm{GPa}$, $v_\mathrm{s} = 0.3$, $v_\mathrm{c} = 0.2$, $E_\mathrm{c} = 4700 f'_\mathrm{c}{}^{0.5}$ MPa) show that the abscissa ξ_0 and the ordinate η_0 at Point A in Fig. 20 can be described as a function of global confinement factor $\xi = \xi_\mathrm{s} + \xi_\mathrm{cf}$ suggested by Wang and Shao (2014) as follows:

$$\xi_0 = 1 + 0.14\xi^{-1}, \quad \eta_0 = \begin{cases} 0.5 - 0.318\xi & (\xi \leq 0.4) \\ 0.1 + 0.13\xi^{-0.81} & (\xi > 0.4) \end{cases}$$
(9)

The $N_\mathrm{bc}/N_\mathrm{u}$-$M_\mathrm{bc}/M_\mathrm{u}$ curve can be approximately divided into two stages, and they can be described mathematically as follows:

Stage C-D ($N_\mathrm{bc}/N_\mathrm{u} \geq 2\eta_0$)

$$N_\mathrm{bc}/N_\mathrm{u} + aM_\mathrm{bc}/M_\mathrm{u} = 1$$
(10)

Stage C-A-B ($N_\mathrm{bc}/N_\mathrm{u} < 2\eta_0$)

$$-b(N_\mathrm{bc}/N_\mathrm{u})^2 - cN_\mathrm{bc}/N_\mathrm{u} + M_\mathrm{bc}/M_\mathrm{u} = 1$$
(11)

where $a = 1 - 2\eta_0$, $b = (1 - \xi_0)/\eta_0{}^2$ and $c = 2(\xi_0 - 1)/\eta_0$.

Considering the influence of the slenderness ratio of the specimen (φ, stability coefficient of the S-CF-CFRP-ST proposed by Wang et al. (2015)), the coupled equation $N_\mathrm{bc}/N_\mathrm{u}$-$M_\mathrm{bc}/M_\mathrm{u}$ of the S-CF-CFRP-ST beam-column is obtained as follows:

$$\begin{cases} \dfrac{1}{\phi}\dfrac{N_\mathrm{bc}}{N_\mathrm{u}} + \dfrac{a}{d}\dfrac{M_\mathrm{bc}}{M_\mathrm{u}} = 1 & \left(N_\mathrm{bc}/N_\mathrm{u} \geq 2\phi^3\eta_0\right) \\ -b\left(\dfrac{N_\mathrm{bc}}{N_\mathrm{u}}\right)^2 - c\dfrac{N_\mathrm{bc}}{N_\mathrm{u}} + \dfrac{1}{d}\dfrac{M_\mathrm{bc}}{M_\mathrm{u}} = 1 & \left(N_\mathrm{bc}/N_\mathrm{u} < 2\phi^3\eta_0\right) \end{cases}$$
(12)

where $a = 1 - 2\varphi^2\eta_0$, $b = (1 - \xi_0)/(\varphi^3\eta_0{}^2)$, and $c = 2(\xi_0 - 1)/\eta_0$.

$1/d$ in Eq. (12) is an enlarged coefficient of the moment considering second order effect, and d is calculated from the following equation:

$$d = 1 - 0.25\left(N_\mathrm{bc}/N_\mathrm{E}\right)$$
(13)

where N_E is the critical Euler load calculated from the following equations:

$$N_\mathrm{E} = \pi^2 E_\mathrm{cfsc} A_\mathrm{cfsc}/\lambda^2$$
(14)

$$E_\mathrm{cfsc} = f_\mathrm{cfscp}/\varepsilon_\mathrm{cfscp}$$
(15)

$$f_\mathrm{cfscp} = \left[0.263\left(f_\mathrm{y}/235\right) + 0.365\left(30/f_\mathrm{cu}\right) + 0.104\right]f_\mathrm{cfscy}$$
(16)

$$f_\mathrm{cfscy} = (1.18 + 0.85\xi)f_\mathrm{ck}$$
(17)

$$\varepsilon_\mathrm{cfscp} = 3.01 \times 10^{-6} f_\mathrm{y}$$
(18)

where E_cfsc is the elastic modulus of the S-CF-CFRP-ST member, A_cfsc is the cross-sectional area of the member, f_cfscp and $\varepsilon_\mathrm{cfscp}$ are the nominal compressive proportional limit stress and its corresponding strain of the S-CF-CFRP-ST, f_cfscy is the axial compressive strength of the S-CF-CFRP-ST stub column (Wang and Shao 2014).
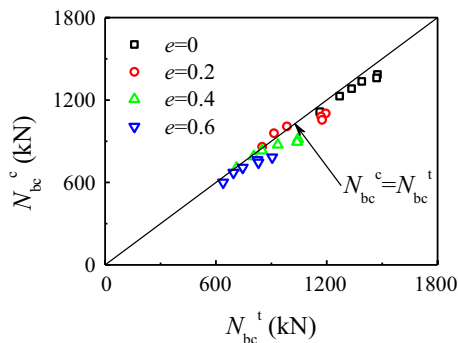
Fig. 23 Comparison between N_{bc}^c and N_{bc}^t

4.2 Validation of Expression

The comparison between the calculated (N_{bc}^c) and tested values (N_{bc}^t) for N_{bc} is shown in Fig. 23. The average value of N_{bc}^c/N_{bc}^t is 0.946, and the mean square error is 0.046, which indicates that the two results agree well.

5 Conclusions

The following conclusions can be drawn based on the presented study: (1) The axial compression-deflection curves on the cross-section at the mid-height of the S-CF-CFRP-ST beam-columns can be classified into elastic stage, elasto-plastic stage and failure stage. (2) The steel tube and the CFRPs can cooperate longitudinally and transversely during the loading process, and the distribution of the longitudinal strains in the steel tube over the depth of the mid-height cross-section is satisfied with the plane section assumption. Moreover, the steel tube under longitudinal tension has little transverse confinement effect on the concrete. (3) The results of parametric analyses show that the yield strength of steel, the strength of concrete and the steel ratio increase can both improve the load-carrying capacity of the S-CF-CFRP-ST beam-columns significantly. The increase in the steel ratio can enhance the stiffness of the elastic stage to some degree. The load-carrying capacity and the stiffness of the elastic stage will reduce significantly, while the slenderness ratio or eccentricity ratio increases. In addition, the variation of the slenderness ratio influences the shape of the N-u_m curves of the S-CF-CFRP-ST beam-columns. (4) Coupled equations for calculating the load-carrying capacity of the S-CF-CFRP-ST beam-columns are proposed, and they are verified to be accurate.

Declarations

Conflict of interest On behalf of all authors, the corresponding author states that there is no conflict of interest.

References

Abdel-Rahman N, Sivakumaran KS (1997) Material properties models for analysis of cold-formed steel members. J Struct Eng 123(9):1135–1143

Al Zand AW, Badaruzzaman WHW, Mutalib AA, Qahtan AH (2015) Finite element analysis of square CFST beam strengthened by CFRP composite material. Thin-Walled Struct 96(1):348–358

Al Zand AW, Badaruzzaman WHW, Mutalib AA, Hilo SJ (2016) The enhanced performance of CFST beams using different strengthening schemes involving unidirectional CFRP sheets: an experimental study. Eng Struct 128(1):184–198

Cai ZK, Wang DY, Smith ST, Wang ZY (2016) Experimental investigation on the seismic performance of GFRP-wrapped thin-walled steel tube confined RC columns. Eng Struct 110(1):269–280

Che Y, Wang QL, Shao YB (2012) Compressive performances of the concrete filled circular CFRP-steel tube (C-CFRP-CFST). Adv Steel Constr 8(4):311–338

Dai Y, Zhao J (2018) Bearing capacity analysis of concrete filled steel tubular composite columns strengthened with CFRP and angle steel under axial compression. Archit Struct 48(17):96–103

Karren KW (1967) Corner properties of cold-formed steel shapes. J Struct Div 93(1):401–432

Li DS, Du FZ, Chen Z, Wang YL (2016) Identification of failure mechanisms for CFRP-confined circular concrete-filled steel tubular columns through acoustic emission signals. Smart Struct Syst 18(3):525–540

Li N, Lu YY, Li S, Liu L (2018) Slenderness effects on concrete-filled steel tube columns confined with CFRP. J Constr Steel Res 143(1):110–118

Nie JG, Wang YH, Fan JS (2014) Seismic behavior of concrete filled steel tubular columns under pure torsion and compression torsion loads (1st edition). Chinese J Civil Eng 47(1):47–58

Park JW, Hong YK, Choi SM (2010) Behaviors of concrete filled square steel tubes confined by carbon fiber sheets (CFS) under compression and cyclic loads. Steel Compos Struct 10(2):187–205

Park JW, Hong YK, Hong GS, Kim JH, Choi SM (2011) Design formulas of concrete filled circular steel tubes reinforced by carbon fiber reinforced plastic sheets. Procedia Eng 14:2916–2922

Sundarraja MC, Ganesh PG (2011) Investigation on strengthening of CFST members under compression using CFRP composites. J of Reinf Plast Compos 30(15):1251–1264

Sundarraja MC, Ganesh PG (2012) Experimental study on CFST members strengthened by CFRP composite under compression. J Constr Steel Res 72(5):75–83

Tao Z, Han LH, Zhuang JP (2007a) Axial loading behavior of CFRP strengthened concrete-filled steel tubular stub columns. Adv Struct Eng 10(1):37–46

Tao Z, Han LH, Wang LL (2007b) Compressive and flexural behaviour of CFRP repaired concrete-filled steel tubes after exposure to fire. J Constr Steel Res 63(8):1116–1126

Wang QL, Chen XY (2014) Static behavior of concrete filled square steel tubular columns strengthened with carbon fiber (I)—experimental study and finite element simulation. Ind Build 44(07):141–145

Wang QL, Niu XJ (2017) Parametric analysis and restoring force model of circular CFRP concrete filled steel tubular columns. Eng Mech 34(S1):159–166

Wang QL, Shao YB (2014) Compressive performances of concrete filled square CFRP-steel tubes (S-CFRP-CFST). Steel Compos Struct 16(5):455–480

Wang QL, Shao YB (2015) Flexural performance of circular concrete filled CFRP-steel tubes. Adv Steel Constr 11(2):127–149

Wang YH, Sw Hu (2019) Mechanical properties of marine structure CFRP Circular restrained concrete filled steel tubular columns under bending and torsion loading. Eng Mech 36(08):96–105

Wang QL, Li J, Shao YB, Zhao WJ (2015) Flexural performances of square concrete filled CFRP-steel tubes (S-CF-CFRP-ST). Adv Struct Eng 18(8):1319–1344

Wang QL, Qu SE, Shao YB, Feng LM (2016) Static behavior of axially compressed circular concrete filled CFRP-steel tubular (C-CF-CFRP-ST) columns with moderate slenderness ratio. Adv Steel Constr 12(3):263–295

Wang JF, Shen QH, Wang FQ, Wang W (2018) Experimental and analytical studies on CFRP strengthened circular thin-walled CFST stub columns under eccentric compression. Thin-Walled Struct 127(1):102–119

Yuan H (2016) Quasi-static research on seismic performance of steel bridge piers with thin-wall ribbed square cross section. J Fuzhou Univ 44(4):459–464